Improved Delayed Detached Eddy Simulation of the Slipstream and Trackside Pressure of Trains with Different Horizontal Profiles

M. Li[1], B. Liu[1], T. H. Liu[2,3,4] and Z. J. Guo[2,3,4†]

[1] *P&T Research Center, CRRC Tangshan Co., Ltd., Tangshan 063035, China*
[2] *Key Laboratory of Traffic Safety on Track of Ministry of Education, School of Traffic & Transportation Engineering, Central South University, Changsha 410075, China*
[3] *Joint International Research Laboratory of Key Technology for Rail Traffic Safety, Central South University, Changsha 410075, China*
[4] *National & Local Joint Engineering Research Centre of Safety Technology for Rail Vehicle, Central South University, Changsha 410075, China*

†*Corresponding Author Email: gszxgzj@csu.edu.cn*

ABSTRACT

The slipstream caused by high-speed trains may harm pedestrians and workers trackside. In general, the characteristics of the slipstream are influenced mainly by the nose shape of the train. The present study explores the slipstream caused by high-speed trains with three different horizontal nose profiles based on the results of three-dimensional, improved delayed detached eddy simulation (IDDES) with an unsteady turbulence model and a set of 1/8th scaled train models. The results obtained using this numerical methodology are in good agreement with those obtained from corresponding wind tunnel tests. The trackside pressure changes around the train models are also captured and analyzed. The analysis reveals that the width of the nose can significantly influence the magnitude and arrival time of slipstream velocity and pressure peaks. The results and proposed numerical methodology can be used as guidelines for the design of high-speed train nose shapes.

Keywords: High-speed train; Improved delayed detached eddy simulation (IDDES); Nose shape; Slipstream; Trackside pressure.

NOMENCLATURE

$c_{\Delta p}$	coefficient of the peak to peak pressure	TOR	Top of Rail
c_p	coefficient of the pressure	CFD	Computational Fluid Dynamics
COT	center of Track	u_{in}	inlet velocity
DES	detached Eddy Simulation	U	time-averaged normalized velocity of the slipstream
DDES	delayed Detached Eddy Simulation		
IDDES	improved Delayed Detached Eddy Simulation	u	time-averaged normalized longitudinal velocity
LES	large Eddy Simulation	v	time-averaged normalized lateral velocity
EN	kinetic Energy of turbulence	w	time-averaged normalized vertical velocity
p_0	atmospheric pressure	ρ	air density at 20°C
P	mean pressure		
RANS	Reynolds-Averaged Navier-Stokes		

1. INTRODUCTION

Railway transportation is becoming an increasingly common mode of transportation owing to its economical and environmentally friendly characteristics. This is particularly the case for railway transportation involving high-speed trains. Steadily increasing train speeds and more complicated operating conditions have led to an increasing amount of research regarding the

aerodynamics of the trains. In this regard, the nose region of a train is well known to have the most obvious effect on the surrounding fluid fields, and the effects of nose shape on the aerodynamic performance of high-speed trains have become a focus of researchers worldwide (Hemida and Krajnovic, 2008; Chen *et al.,* 2018).

The nose geometry of high-speed trains can affect the aerodynamic performance of high-speed trains under different operating conditions by changing the flow field around them. Chen *et al.* (2016) studied the aerodynamics of three train models having heads with different streamline lengths and identical cross sections in open air conditions without a crosswind and found that increasing the nose length from 5 m to 15 m decreased the total drag by 22.4%, and the vortex shedding strength and the wake flow were substantially weakened. Chen *et al.* (2017) employed the DES method to analyze changes in the trackside pressure caused by trains with different nose lengths according to the EN standard requirement and demonstrated that the maximum $c_{\Delta p}$ value decreased with increasing nose length in a quadratic polynomial relationship. A number of researchers have also investigated reducing the aerodynamic drag of trains by optimizing the shape of the nose (Li *et al.,* 2016; Zhang *et al.,* 2018). Hemida and Krajnovic (2008) studied crosswind flows around two high-speed trains with different nose shapes using LES. Their results captured a highly unsteady and three-dimensional (3D) flow around the nose that yielded a greater number of vortex structures in the wake around the short nose train model and which further influenced the side force, the lift force, as well as the dominating frequency of the aerodynamic forces on the train. Later, Hemida and Krajnović (2010) again adopted LES to study the influence of nose shape and yaw angle on the flow structures around trains. Their results indicated that the nose shapes of the train models employed in their study could have a substantial effect on both the time-averaged and instantaneous wake flows. Chen *et al.* (2018) investigated the aerodynamic performance of trains having heads with different streamline lengths of 4 m, 7 m, 9 m, and 12 m under crosswind conditions. Increasing the nose length of the train from 4 m to 12 m decreased the drag coefficient of the train by 19.0%, and the side force and lift and roll moment coefficients decreased by 10.6%, 21.7%, and 7.3%, respectively. In addition, the nose length was found to impact the value of c_p noticeably on both the windward side of the head car and the leeward part of the tail car. Zhang *et al.* (2018) sought to improve the aerodynamics of high-speed trains under crosswind conditions by conducting an optimization of the nose shape using seven optimization design variables. The total aerodynamic drag force of the train model with the optimized nose shape decreased by 2.63%, the aerodynamic lift force of the head coach decreased by 9.51%, and the aerodynamic side force of the head coach decreased by 2.06%. Nose shape is also an important factor affecting numerous aerodynamic parameters for trains operating in

tunnels, such as the aerodynamic forces, pressure changes on the train surface and the tunnel wall, and micro-pressure waves (Chen *et al.,* 2017; Kwak *et al.,* 2013; Lee and Kim, 2008; Li *et al.,* 2017).

In addition to basic aerodynamic concerns, the movement of a high-speed train can generate a slipstream and pressure fluctuations in the surrounding air, which in turn generate forces acting on nearby pedestrians and stationary objects, as well as on trackside workers, and can result in injury and damage to railway infrastructure (Baker, 2010; Flynn *et al.,* 2016). For example, more than 20 accidents, which mainly involved wheeled items positioned on station platforms, as well as travelers and their belongings, have been recorded in the UK during the period 1972 to 2005, and an increasing trend in the number of accidents has been observed (Flynn *et al.,* 2014). In general, the slipstream and pressure fluctuations around a moving train are affected by many factors, such as the distances from the TOR and the COT, the velocity of the train, as well as the aerodynamic characteristics of geometric features (EN, 2010). Hemida *et al.* (2010) investaged that the velocity of the slipstream is almost linearly proportional factor the speed of the train. It has also been demonstrated that the nose shape is also an important factor affecting the characteristics of the slipstream. The slipstream obtained using different train models has been investigated in recent years, and the results have been found to vary depending on the type of model employed (Sterling *et al.,* 2008; Herbst *et al.,* 2012). For example, Flynn *et al.* (2014) calculated the slipstream of a Class 66 locomotive with four type B container wagons in tow. The velocity of the slipstream was found to be much greater than that of the CRH2 trains obtained by Huang *et al.* (2016) due to the blunt geometric profile of the locomotive, and the slipstreams caused by these two trains also differed from that obtained by Hemida and Krajnović (2010) for an ICE train. Guo *et al.* (2018) compared the slipstreams caused by single- and double-unit trains and found that the slipstream and the surrounding pressure distributions were quite different due to the two extra streamlined noses at the middle of the double-unit train. Xie *et al.* (2018) calculated the slipstream and the trackside pressure changes generated by a set of trains with different longitudinal section lines. The results indicated that the variations in the slipstream velocities and trackside pressures with respect to the peak locations induced by the four types of trains were similar, while their amplitudes were different. The differing amplitudes were attributed to the various slopes of the longitudinal section lines. The horizontal nose profiles of trains also change the relative distance between the train and the platform, which may give an important influence on the slipstream. However, it seems to be rarely studied.

The present work focuses on the slipstream characteristics generated by three 1/8th scaled train

models with different horizontal profiles using the IDDES method. The numerical results are verified by comparison with the results of wind tunnel tests conducted with equivalently scaled train models. The remainder of this paper is organized as follows. The geometrical shapes of the trains are presented in Section 2. The numerical methodology, the computational domain, the boundary conditions, and the computational meshes are described in Section 3. The verification of the numerical accuracy is presented in Section 4. The slipstream and the pressure surrounding the train models are presented in Section 5. Finally, Section 6 presents the conclusions of the study.

2. GEOMETRICAL SHAPES OF THE TRAIN MODELS

Standard modifications to the shape of the nose mainly focus on controlling the characteristic lines and free deformation of the models. The characteristic lines are mainly controlled in terms of the two-dimensional (2D) profile line, which then forms a set of 3D models. This modification method is mainly applied to basic research focused on evaluating the influence of head shape parameters on the mechanisms affecting aerodynamic performance. Free deformation is an algorithm-based computer-controlled free form method that directly alters the geometry of the nose and is mainly used to optimize specific train models. Therefore, the present work uses three train models with equivalent shape parameters and different horizontal profile lines.

In general, the aerodynamic performance of a train get worse as the nose width of the train will have. However, an overly narrow nose structure may result in insufficient space for mechanical components and an insufficient view angle for the front window of the head car, which would detrimentally affect the normal operation of the train. Therefore, an appropriate base nose width should be selected according to the designed speed and other operating conditions of the train, and appropriate adjustments made in terms of the horizontal contour for evaluating the slipstream and frequency characteristics generated by these trains with different nose widths. As shown in Fig. 1, we employ streamlined train model B with a streamline length of 9 m as the base nose shape and modify this base case through two horizontal section lines as the two nose shapes B−1 and B+1. Figure 2 presents front views of the three nose shapes. It should be noted here that all three train models have the same longitudinal 2D contour, and all other parameters, such as the streamline length (9 m) and total train length (75.6 m), remain unchanged except for the nose widths. Each train model consists of three cars, including a head car, an intermediate car, and a tail car, and incorporates the bogie and the gap of the cars, which are provided according to their standard designs. In addition, small objects with complex structures, such as roof pantographs, train lights, and handles, are omitted to conserve computational resources.

3. NUMERICAL SIMULATION MODEL

3.1 Mathematical Model

The slipstream caused by trains and its frequency characteristics are fluid parameters that depend highly on transient calculations, which are difficult to capture accurately using time-averaged simulations such as RANS simulations. In contrast, LES is widely agreed to be a high precision turbulence model, but which generally has high grid density and computational resource requirements that greatly increase the computational burden. The disadvantages of RANS and LES can be mitigated by DES, which is a mixture of the two turbulence models, where RANS is adopted to approximate the mean boundary layer behavior, and LES is applied to capture the time-dependent flow at a distance from wall boundaries. Researchers have widely employed DES to study the aerodynamic performance of trains under a great number of different running conditions (Flynn *et al.*, 2014; Zhang *et al.*, 2016; Muld *et al.*, 2014).
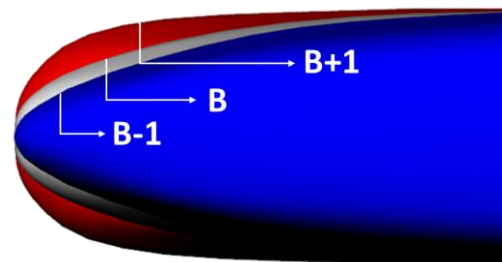
Fig. 1. Horizontal nose profiles of the high-speed train models employed in the present work.
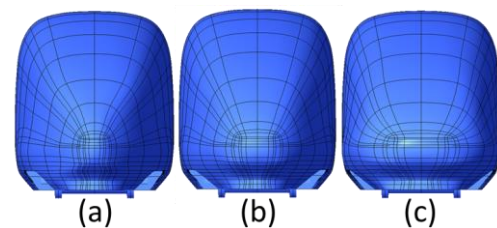
Fig. 2. Front views of the different high-speed train nose shapes: (a) B−1; (b) B; (c) B+1.

However, DES has a few shortcomings. For example, thickening in the upper regions of boundary layers has been found to promote early flow separation owing to a premature switch between the RANS and LES modes in this region, which leads to modeled stress depletion (MSD) and grid-induced separation (GIS). This issue has been addressed to some extent by the development of DDES. In addition, IDDES is a relatively new method that combines DDES and wall-modeled LES (WMLES). Here, IDDES eliminates the suboptimal performance of DES associated with MSD and GIS and further promises to reduce the Reynolds numbers
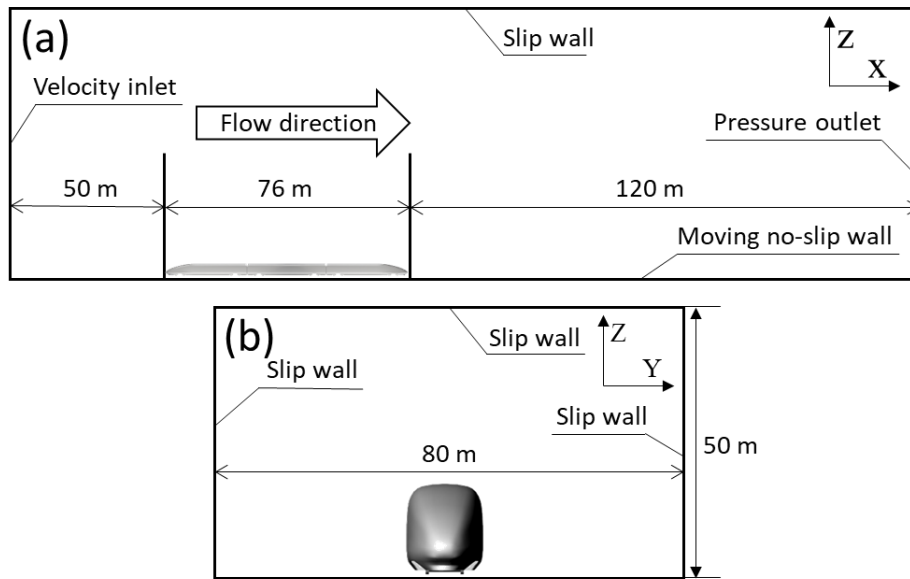
Fig. 3. Computational domain and boundary conditions: (a) side view; (b) front view.

dependence and the high levels of resolution required for conducting classic LES in turbulent boundary layers. The IDDES model based on k-ω equations is adopted in the present work with a time step of 5.0 μs.

3.2 Computational Domain and Boundary Conditions

The train model is positioned in the computational domain according to the illustration given in Fig. 3. The upstream distance between the inlet boundary and the nose of the train model is 50 m, and the downstream distance between the outlet boundary and the tail nose is set as 120 m. The width of the domain is 80 m, and the model is at the center of the spanwise direction. This domain has a height of 50 m. A velocity inlet is utilized at the inlet boundary, and the velocity is set equal to the velocity of the train. The outlet is set to a zero-pressure surface. Sliding wall conditions are used on the upper surface and both sides. A moving no-slip wall is utilized on the lower surface to reproduce the relative motion between the train and the ground.

3.3 Computational Mesh

The SnappyHexMesh program included in the open source software package OpenFOAM was used for generating the unstructured hexahedral meshes in this study. To ensure that the final solution is not a function of mesh density, a grid-dependence test was conducted for the base model B prior to conducting calculations. Coarse and fine meshes consisting of 14 million and 20 million cells, respectively, were generated using different parameters. The primary details of these two grid configurations are outlined in Table 1. We note from the table that the minimum cell size of the

coarse mesh on the train surface is twice that of the fine mesh. The number of the prism layers is kept constant, while the thickness of the first boundary layer of the coarse mesh is also twice that of the fine mesh due to the different surface grid sizes.

Table 1 Parameters of the coarse and fine mesh configurations for the grid-dependence testing of train model B

	Coarse	Fine
Total number of cells	1,3663,356	20,379,562
Minimum cell size on the train surface (mm)	4.6	2.3
Number of prism layers	10	10
Thickness of the first boundary layer (mm)	0.46	0.23

An intuitive contrast between the two meshes can be obtained by plotting *U*, which is time-averaged according to the EN standard at 3.0 m from the COT and 1.44 m from the TOR as a function of distance from the nose of the head car in Fig. 4. Here, *U* is defined as

$$U = \frac{\sqrt{(u - u_{in})^2 + v^2 + w^2}}{u_{in}} . \tag{1}$$

where *u, v, w* is the velocity components in the longitude, lateral, and vertical directions of the simulated airflow, respectively, and u_{in} is the uniform velocity of the inlet.
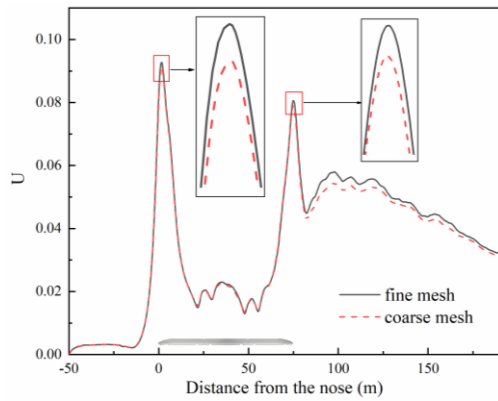
Fig. 4. Mesh sensitivity of the time-averaged magnitude of the normalized velocity of the slipstream (*U*) for coarse and fine meshing with respect to the distance from the nose of the head car.

As illustrated in Fig. 4, the differences in the values of *U* obtained using the coarse and the fine meshing are not significant. Here, the differences in *U* at the head nose and the tail nose are less than 1.55%. This is a satisfying result because the fine mesh is not required to resolve the majority of the important fluid structures. Hence, the coarse meshing was employed for all subsequent calculations. Figure 5 illustrates the meshing of train model B employed in the present work.
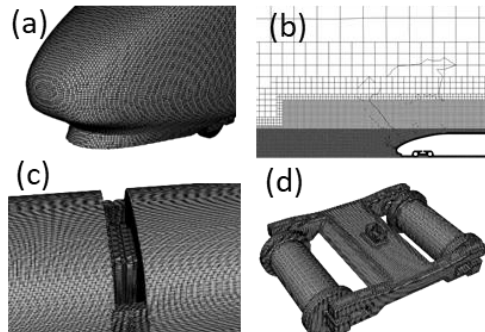
Fig. 5. Computational mesh employed in the simulations: (a) mesh distribution around the head car; (b) varying mesh density in the computational domain; (c) mesh distribution around the gap; (d) mesh distribution at the bogie.

4.   MODEL VALIDATION

A set of wind tunnel tests were conducted at the China Aerodynamic Research and Development Center. The wind tunnel facility, model train, and pressure monitoring points are shown in Fig. 6(a), (b), and (c), respectively. The actual size of the wind tunnel is 8 m × 6 m. The tests employed a Chinese CRH2 train model with a 1/8th scale according to block ratio requirements, which should be less than 5%. The ballast model with a single track has a length of 15.2 m under the same 1/8th scale and was

mounted on a rotatable disk. The train models were hollow, and three force balances were used to test the aerodynamic force of the model train cars. The longitudinal symmetric plane of the train model was selected for pressure monitoring, and a set of pressure taps were accordingly located on curve 1 of the head and tail cars [more information regarding the wind tunnel tests can be found in the work of Zhang *et al.* (2018)]. The data sampled during testing were recorded by a VXI multi-channel recording system. In addition, Fig. 6(d) illustrates that the train model employed in the validation simulations is fully comparable to that of the wind tunnel tests [see Fig. 6(b)], and the size of the computational domain and the boundary conditions are also equivalent. The Reynolds number was approximately 1.89×10^6 for both wind tunnel tests and simulations.

Figures 7(a) and (b) present the values of c_p obtained on curve 1 of the head and tail cars, respectively, during the wind tunnel test and by numerical simulation. Here, c_p is defined as

$$c_p = \frac{P - P_0}{\frac{1}{2}\rho u_{in}^2}, \qquad (2)$$

where P denotes the absolute surface pressure, P_0 is the pressure of the atmosphere, and ρ is the density of air at 20°C.

The figures indicate that a good agreement is obtained between the numerical and experimental data. The largest discrepancies occur at the transitions from the streamlined structure to the top plane of the train (i.e., at pressure taps H8, H9, and H10 of the head nose and taps T2 and T3 of the tail nose). The discrepancies between the simulation and experimental data could be related to the incomplete consistency of geometrical factors (such as roughness) between the CFD models and the physical model.

5.   RESULTS AND DISCUSSION

5.1   Time-Averaged   Velocity   of   the Slipstream

To meet the assessment criteria of the EN standard, a considerable amount of the instantaneous IDDES data was used and sampled to obtain the time-averaged velocity of the slipstream at 3.0 m from the COT, 0.2 m from the TOR and 3.0 m from the COT, 1.44 m from the TOR. These positions are illustrated with respect to the train body in Fig. 8.

Figure 9 presents the values of the *U* obtained for the three train models at 3.0 m from the COT, 0.2 m from the TOR. We note that *U* is constant at the upstream region far away from the nose for all train models and that the value of *U* increases continuously while approaching the nose area, where the air around the nose is pushed ahead and aside. However, the maximum amplitude of *U* at the nose varies among the three train models considered. Here, model B+1, which has the widest nose, has the largest maximum amplitude of *U* at the nose compared to the other two train models, as shown by the inset on
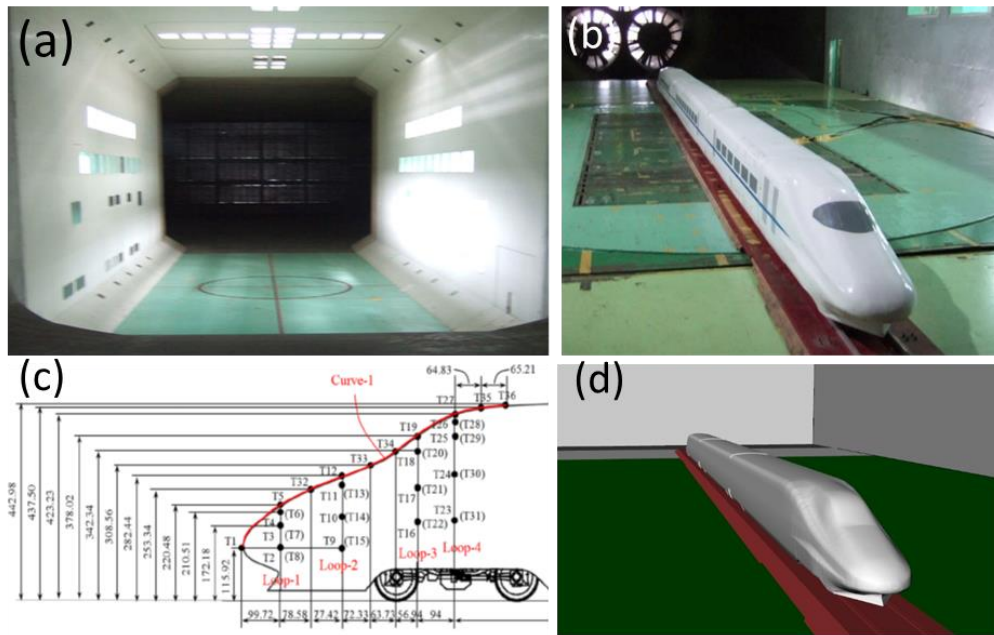
Fig. 6. Wind tunnel tests: (a) test section of the wind tunnel; (b) the CRH2 train and rail models; (c) positions of the monitor sensors; (d) simulation under equivalent conditions.
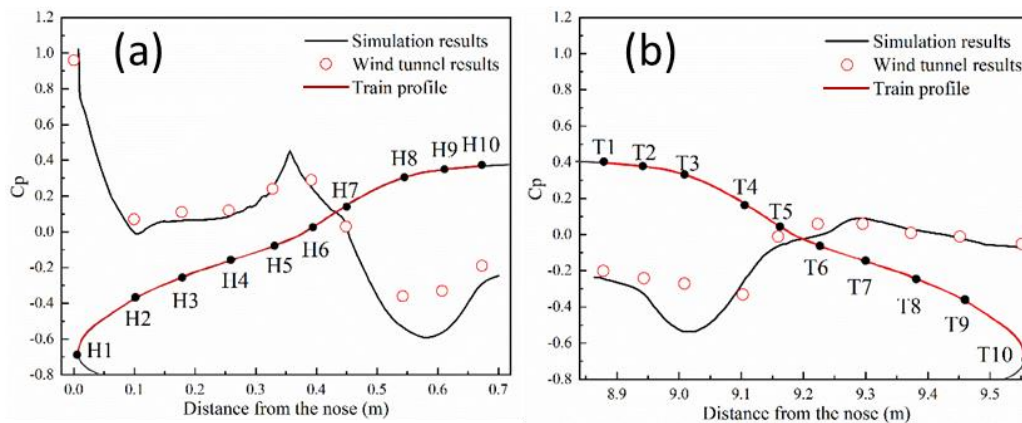
Fig. 7. Comparison of calculated and experimental results of the pressure coefficient (c_p) on the train surface with respect to the distance from the nose: (a) at curve 1 on the head car; (b) at a symmetrical curve on the tail car.

the left-hand side in Fig. 9. In addition, we note that the maximum amplitude of U is slightly greater for model B than that for model B−1. It is also noted that the position of the maximum with respect to the nose tip varies for the three train models. Here, the maximum amplitude of U appears first for model B+1 while approaching the nose region from the upstream direction, which is followed by that of base model B and, finally, by that of model B−1, which has the narrowest nose. This is because the value of U was monitored at the same position (i.e., 3.0 m from the COT, 0.2 m from the TOR), while the width of the noses is different, so that the actual reference distance from this monitoring point to the train nose surface differs for the three models. This orderly positioning of the maximum amplitude of U can therefore be easily explained by the fact that the widest train model is first to

present its widest profile, which represents the smallest reference distance, so that model B+1 is first to present a maximum amplitude of U while approaching the nose region. This can also be illustrated by the streamlines around the train models within a horizontal plane 1.44 m from the TOR, as shown in Fig. 10. Most of these streamlines are quite similar, except for those within the area denoted by the rectangle outlined by the black dotted line. Here, model B+1 results in greater deformation and distortion of the streamlines. This can be quantitatively analyzed by selecting the same number of streamlines at the nose tip (i.e., at $x = 0$ along the dotted blue line in Fig. 10) for models B−1, B, and B+1 and defining their widths as d_{B-1}, d_B, and d_{B+1}, respectively. Accordingly, these values can be ordered as d_{B+1}, d_B, d_{B-1} when sorted from
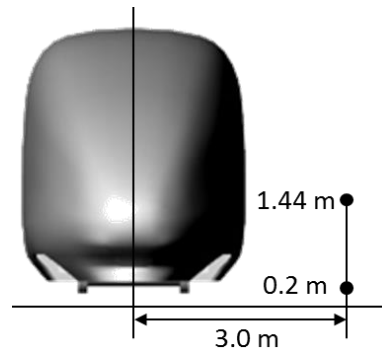
Fig. 8. Positions of points required by the EN standard for measuring *U*.
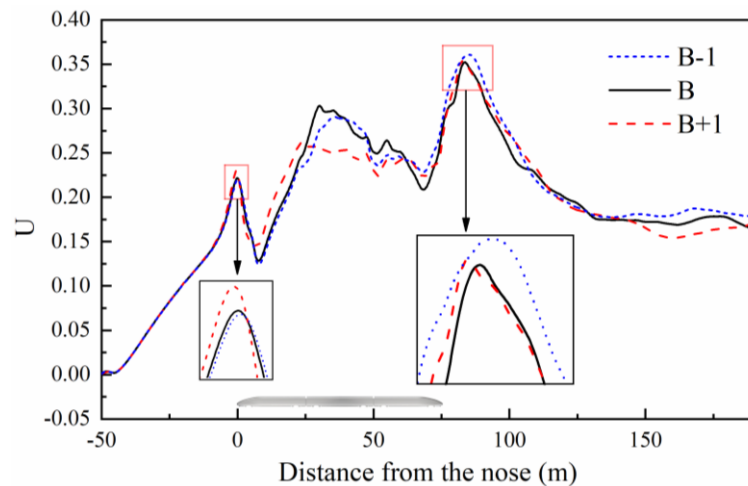
Fig. 9. Values of *U* for the different train models at 3.0 m from the COT and 0.2 m from the TOR with respect to the distance from the nose.
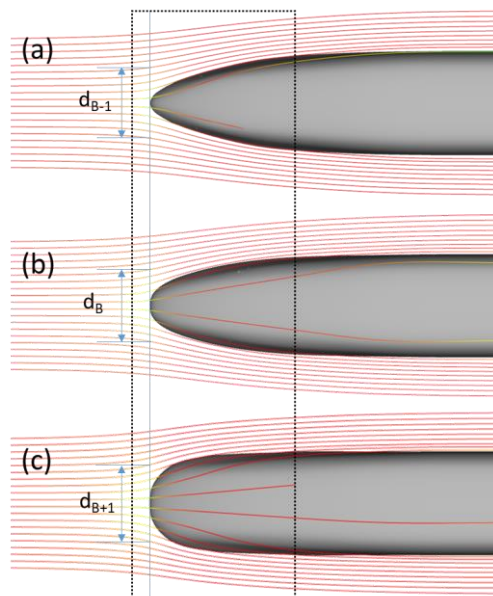
Fig. 10. Streamlines around the three train models within a horizontal plane located at 1.44 m from the TOR: (a) B−1; (b) B; (c) B+1.

high to low, which matches with the position at which the maximum amplitude of *U* was obtained, as discussed above.

To facilitate a deeper understanding of the above-discussed phenomenon, the normalized velocities of the simulated airflow in the longitudinal, lateral, and

vertical directions are presented in Figs. 11(a), (b), and (c), respectively. Here, we note that different ranges are employed on the ordinate axes to make better use of the figures. Overall, the values of the longitudinal velocity component are the largest, followed by those of the lateral component, and, finally, by the values of the vertical component. The increase in U for all train models can be attributed completely to changes in the longitudinal velocity component far in advance of the nose tip in the upstream region. The abrupt changes near the head nose and tail nose are regarded as the collective effect of longitudinal and lateral velocity components. We also note that the velocity component values of train models B and B−1 are quite similar throughout all regions of the simulated domain.
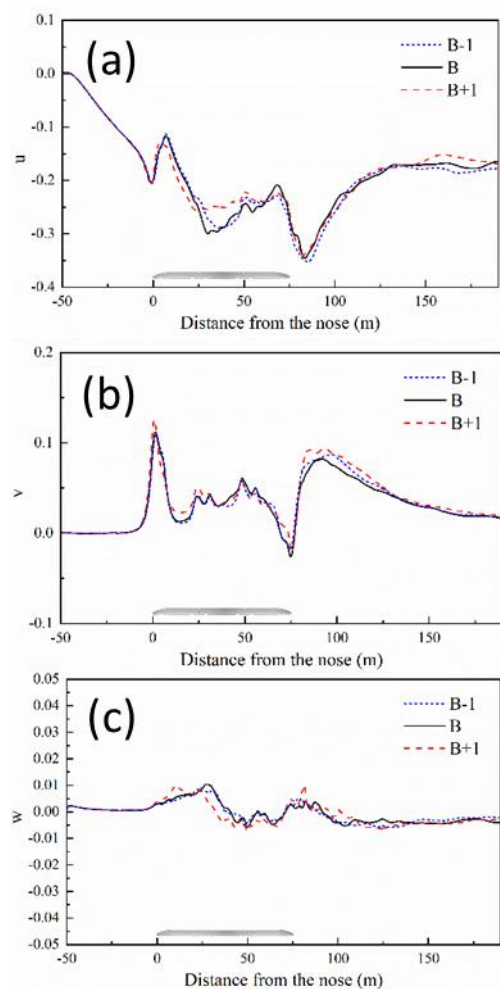
Fig. 11. Time-averaged magnitudes of the normalized velocity components for the different train models at 3.0 m from the COT and 0.2 m from the TOR: (a) longitudinal velocity, *u*; (b) lateral velocity, *v*; (c) vertical velocity, *w*.

With respect to the normalized values of *u* in Fig. 11(a), the three models present nearly equivalent values leading up to the nose tip. Then, the values of *u* continuously increase until passing beyond the head car, after which they decrease. Subsequently,

the normalized value of *u* for model B+1 remains fairly constant, while these values continue to decrease for the other two models, and then finally increase again until all models attain similar values from the front of the tail nose to the outlet. In addition, the normalized values of *u* for model B+1 present earlier arriving peaks in different regions, particularly in the near wake region. As for the normalized values of *v* in Fig. 11(b), these values are generally greater for model B+1 over nearly the entire domain, and particularly in the nose region and the near wake region. The peak value of *v* generated by model B+1 is the largest, while this value is smallest for the narrowest model (B−1). It is also noted that, since the peak value of *v* in the wake flow for model B is less than that of B−1, the peak value of *v* in the wake flow cannot be directly correlated with the width of the streamlined structure of the train models. This may be related to the high complexity of the wake flow. The highest normalized value of *w* in Fig. 11(c) occurs when passing the middle cars of models B and B−1, while that of model B+1 occurs earlier, but has a smaller magnitude than that of the other two models. In addition, model B+1 also exhibits a greater value of *w* in the wake flow.
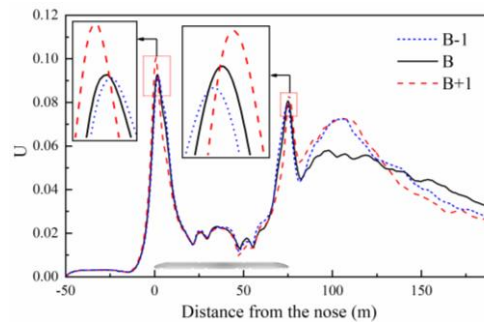
Fig. 12. Time-averaged values of *U* for the different train models at 3.0 m from the COT and 1.44 m from the TOR.

Figure 12 presents the values of the *U* obtained for the three train models at the other measure point (i.e., 3.0 m from the COT, 1.44 m from the TOR). Here, we note that these values are substantially lower than those of Fig. 9, and that the maximum values of *U* appear around the head nose region rather than around the near wake region, as they do in Fig. 9. As shown in the inset on the left-hand side in Fig. 9, the widest train model provides the highest and earliest peak value of *U*, while that of the narrowest train model is the lowest and the latest peak, which is similar to the peak provided by train model B. This behavior is equivalent to that observed at the lower monitoring position ($z = 0.2$ m) shown in Fig. 9. In addition, the value of *U* observed between the head nose and the tail nose at the higher monitoring position ($z = 1.44$ m) shown in Fig. 12 is more stable than that observed in Fig. 9. As shown in the inset on the right-hand side in Fig. 12, the peak values of *U* generated by the three train models when passing the tail car differ substantially, and their relative positions are equivalent to those obtained

Table 2 Peak-to-peak pressure values in the nose region of the head car for the three train models.

z (m)	Peak-to-peak pressure at $y = 2.5$ m					
	1.5	1.8	2.1	2.4	2.7	3.0
B−1	465.0	453.2	441.2	427.8	412.5	395.3
B	449.9	438.0	426.4	414.0	400.0	384.5
B+1	436.8	425.5	413.6	400.6	386.9	372.4

in the nose region. In addition, the relative magnitudes and positions of these peaks also differ from those observed in Fig. 9. These differences can be attributed to the strong turbulent flow at the bottom of the train, which weakens the influence of the slipstream caused by the train models, while no such interference occurs at the higher monitoring position (i.e., $z = 1.44$ m).

The normalized velocities in the longitudinal, lateral, and vertical directions of the computational domain are also plotted for the higher monitoring position in Figs. 13(a), (b), and (c), respectively. Here, we again employ different ranges on the ordinate axes to make better use of the figures. We note that model B+1 provides the lowest peak values of u in Fig. 13(a) at the nose regions of the head and tail, while model B−1 provides the highest values in these two areas. Model B exhibits smoother changes in u at the wake region, which results in the different values of U with that of model B+1 and B−1 shown in Fig. 12. In addition, while only negative values of u occur at the lower monitoring point, both positive and negative values of u are found at the higher monitor point in Fig. 13(a). Compared with the results presented in Fig. 11(b), the normalized values of v shown in Fig. 13(b) are shifted in the negative direction. We also note that the three train models provide very similar normalized values of v. Interestingly, the normalized values of w at z = 1.44 m in Fig. 13(c) are about twice of those obtained at $z = 0.2$ m in Fig. 11(c).

5.2 Time-Averaged Trackside Pressure

The time-averaged trackside pressure is also an important parameter serving as an assessment criterion in the EN standard. The peak-to-peak values, which are the difference between the maximum positive pressure and the maximum negative pressure in the nose region, at 2.5 m from the COT and 1.5–3.0 m (in 0.3 m intervals) from the TOR are listed in Table 2.

As listed in Table 2, the peak-to-peak pressure values in the nose region decrease with increasing distance from the TOR in the z range of 1.5–3.0 m. In addition, the peak-to-peak pressure generated at a given value of z decreases with increasing nose width. The data listed in Table 2 are also plotted in Fig. 14 to provide a more intuitive comparison. From Fig. 14, we note that the peak-to-peak pressure values provided by the three models present approximately linear relationships with respect to the distance from the TOR. In addition, changes in the peak-to-peak pressure around each train model are approximately equal at the different distances from

the TOR, such that the three plots lie parallel to each other.
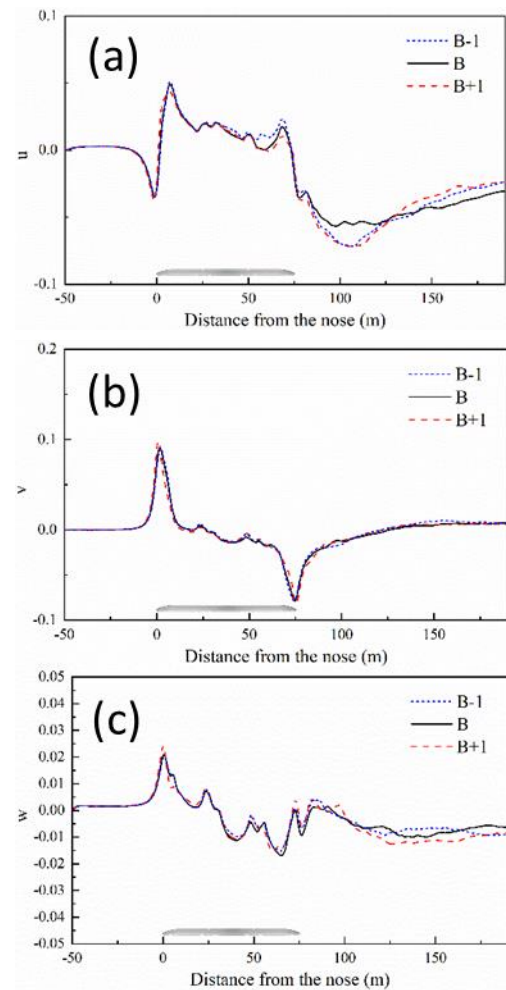
Fig. 13. Time-averaged magnitudes of the normalized velocity components for the different train models at 3.0 m from the COT and 1.44 m from the TOR: (a) longitudinal velocity, *u*; (b) lateral velocity, *v*; (c) vertical velocity, *w*.

Figure 15 presents the time-averaged values of c_p obtained for the three train models at $y = 2.5$ m and z values of 1.5–3.0 m in 0.3 m intervals. Obvious differences in the values of c_p obtained for the three train models are observable in three areas. The first area is the sudden increase in c_p when passing the nose tip, as shown in the insets in the middle of the figures. Here, train model B+1 provides the highest
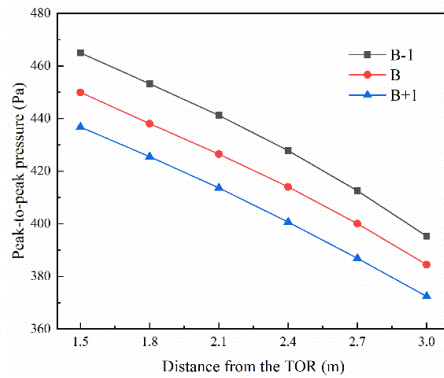
Fig. 14. Peak-to-peak pressure values around the nose (y = 2.5 m) of the three train models.
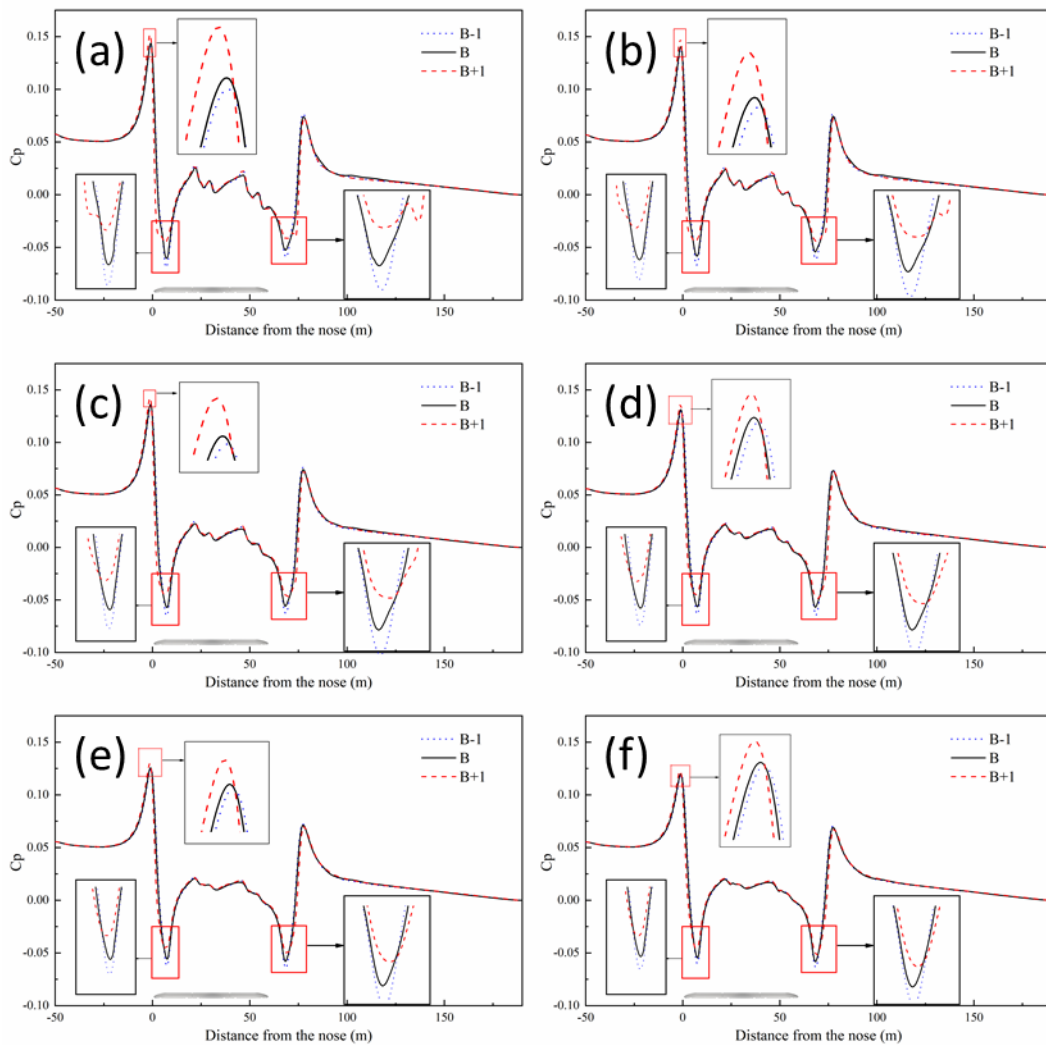
Fig. 15. Time-averaged pressure coefficients (c_p) of the three train models at y = 2.5 m (i.e., distance from the COT) and at z values (i.e., distance from the TOR) of (a) 1.5 m, (b) 1.8 m, (c) 2.1 m, (d) 2.4 m, (e) 2.7 m, and (f) 3.0 m.

positive peak value of c_p, and train model B−1 provides the lowest value. In the second area, the values of c_p decrease sharply over the head car toward negative peak values due to the guidance of the streamlined structure, as shown in the insets on the left-hand side of the figures. Here, the relative magnitudes differ completely from those observed in the first area, where model B−1 generates the largest negative peak value of c_p, which is much more negative than that generated by model B+1. In addition, the differences between the negative peak values of c_p among the train models are also much

greater than the differences observed at the nose tip. Therefore, the negative pressures dominate the peak-to-peak pressure values, which produce the results shown in Table 2 and Fig. 14. However, the time-averaged values of c_p differ little when passing over the main train body. Obvious differences in the values of c_p for the three models finally appear again in the near wake region, as shown in the insets on the right-hand side of the figures. The behavior here in the third region is equivalent to that observed in the second region.

We can also observe differences in the three models from the mean pressure distributions within a horizontal plane at $z = 1.5$ m plotted in Fig. 16. The

mean pressure (Pa)

-1000   -500   0   500   1000
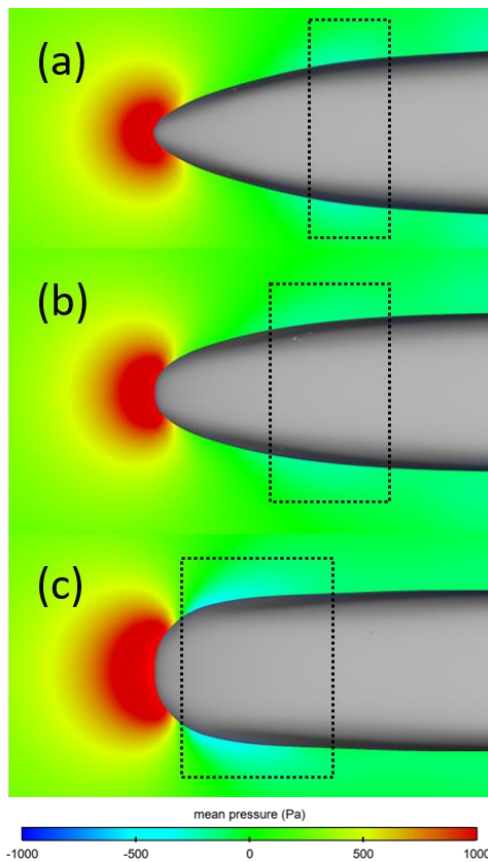
Fig. 16. Pressure distributions around the three train models within a horizontal plane at 1.5 m from the TOR: (a) B−1; (b) B; (c) B+1.

6. CONCLUSIONS

The time-averaged normalized slipstream velocities and pressures around high-speed train models with different horizontal profiles were investigated using a 3D, incompressible IDDES k–ε turbulence model. The numerical model was validated by the good agreement of its results with the results of wind tunnel tests. The monitoring positions considered were mainly those based on the EN standard (i.e., a lower position located at 3.0 m from the COT and 0.2 m from the TOR, and a higher position located at 3.0 m from the COT and 1.44 m from the TOR). The results of this study can be summarized as follows.

first difference is the positive pressure zone formed by the tip of the nose. Here, model B−1 produced a slightly larger positive pressure zone than model B, but the maximum pressure value generated by model B was slightly greater than that of B−1, as reflected by the depth of the color. Of the three models, model B+1 produced the largest positive pressure zone and the highest positive pressure value. The black outlined boxes in Fig. 16 denote the negative pressure zones. As shown in the figure, the blocking effect on the airflow by the geometry of the nose increases as the width of the model increases, resulting in stronger flow separation. Therefore, the range and negative peak pressure value of the region are also increased significantly.

1) At the lower monitoring position, the largest time-averaged value of U appears around the nose tip of the tail car, and the widest train model (B+1) produces the largest value of U at the nose of the tail car and the lowest value of U when passing the middle car. The value of U around the tail car has no obvious regularity and order of appearance, where the narrowest car model (B−1) generates the largest velocity of the slipstream globally.

2) The slipstream generated by the considered train models at the higher monitoring position exhibits better regularity than that at the lower monitoring position, where the values of U generated around the noses of both the head and the tail of the train increase with increasing nose width. In addition, the peak value of U occurs earlier in the upstream direction at the head nose and later in the downstream direction of the tail nose with increasing nose width.

3) The peak-to-peak values of the pressure decrease with increasing nose width. The widest train model forms the highest positive pressure and the lowest negative pressure. In addition, the widest train model generates the largest positive pressure zone in front of the nose tip of the head car and the largest negative pressure zone close to the sides of the nose.

REFERENCES

Baker, C. (2010) The flow around high speed trains. Journal of Wind Engineering and Industrial Aerodynamics. 98(6): 277-298.

Chen, Z., T. Liu, X. Zhou and X. Su (2016). Aerodynamic analysis of trains with different streamlined lengths of heads, Intelligent Rail Transportation (ICIRT), *IEEE International Conference on. IEEE*, 382-387.

Chen, X., T. Liu, X. Zhou, W. H.. Li, T. Xie and Z. Chen (2017). Analysis of the aerodynamic effects of different nose lengths on two trains

intersecting in a tunnel at 350 km/h. *Tunnelling and Underground Space Technology* 66, 77-90.

Chen, Z., T. Liu, X. Chen, T. Xie and W. Li (2017). Comparison of the Trackside Pressure with Respect to Different Nose Lengths of High-Speed Trains. *DEStech Transactions on Engineering and Technology Research.*

Chen, Z., T. Liu, Z. Jiang, Z. Guo and J. Zhang (2018). Comparative analysis of the effect of different nose lengths on train aerodynamic performance under crosswind. *Journal of Fluids and Structures* 78, 69-85.

EN, B. (2010). *14067-6, Railway applications--Aerodynamics Part 4: Requirements and test procedures for aerodynamics on open track*, London: British Standard Institute.

Flynn, D., H. Hemida and C. Baker (2016). On the effect of crosswinds on the slipstream of a freight train and associated effects. *Journal of Wind Engineering and Industrial Aerodynamics* 156, 14-28.

Flynn, D., H. Hemida, D. Soper and C. Baker (2014). Detached-eddy simulation of the slipstream of an operational freight train. *Journal of Wind Engineering & Industrial Aerodynamics* 132, 1-12.

Guo, Z., T. Liu, Z. Chen, T. Xie and Z. Jiang (2018). Comparative numerical analysis of the slipstream caused by single and double unit trains. *Journal of Wind Engineering and Industrial Aerodynamics* 172, 395-408.

Hemida, H. and S. A. Krajnovi (2008). LES study of the influence of a train-nose shape on the flow structures under cross-wind conditions. *Journal of Fluids Engineering* 130, 253-257.

Hemida, H. and S. Krajnović (2010). LES study of the influence of the nose shape and yaw angles on flow structures around trains. *Journal of Wind Engineering and Industrial Aerodynamics* 98, 34-46.

Hemida, H., N. Gil and C. Baker (2010) LES of the slipstream of a rotating train. *Journal of Fluids Engineering* 132(5), 051103.

Herbst, A., T. Muld and G. Efraimsson (2012). *Front Shape and Slipstream for Wide Body Trains at Higher Speeds.* KTH Railway Group, Publication, 1402.

Huang, S., H. Hemida and M. Yang (2016). Numerical calculation of the slipstream generated by a CRH2 high-speed train. *Proceedings of the Institution of Mechanical*

Engineers, Part F: Journal of Rail and Rapid Transit. 230(1), 103-116.

Kwak, M., S. Yun, Y. Lee, H. Kwon, K. Kim and D. Lee (2013). Optimum nose shape of a front-rear symmetric train for the reduction of the total aerodynamic drag. *Journal of Mechanical Science and Technology* 27, 3733-3743.

Lee, J. and J. Kim (2008). Approximate optimization of high-speed train nose shape for reducing micropressure wave. *Structural and Multidisciplinary Optimization* 35, 79-87.

Li, R., P. Xu, Y. Peng and P. Ji (2016). Multi-objective optimization of a high-speed train head based on the FFD method. *Journal of Wind Engineering and Industrial Aerodynamics* 152, 41-49.

Li, W., T. Liu, J. Zhang, Z. Chen, X. Chen and T. Xie (2017). Aerodynamic Study of Two Opposing Moving Trains in a Tunnel Based on Different Nose Contours. *Journal of Applied Fluid Mechanics* 10(5), 1375-1386.

Muld, T. W., G. Efraimsson and D. S. Henningson (2014). Wake characteristics of high-speed trains with different lengths. *Proceedings of the Institution of Mechanical Engineers, Part F: Journal of Rail and Rapid Transit.* 228(4), 333-342.

Sterling, M., C. J. Baker, S. C. Jordan and T. Johnson (2008). A study of the slipstreams of high-speed passenger trains and freight trains. *Proceedings of the Institution of Mechanical Engineers, Part F: Journal of Rail and Rapid Transit* 222(2), 177-193.

Xie, T., T. Liu, Z. Chen, X. Chen and W. Li (2018). Numerical study on the slipstream and trackside pressure induced by trains with different longitudinal section lines. *Proceedings of the Institution of Mechanical Engineers, Part F: Journal of Rail and Rapid Transit* 232, 1671-1685.

Zhang, J., J. Li, H. Tian, G. Gao and J. Sheridan (2016). Impact of ground and wheel boundary conditions on numerical simulation of the high-speed train aerodynamic performance. *Journal of Fluids & Structures* 61(4), 249-261.

Zhang, L., J. Zhang, T. Li and Y. Zhang (2018). A multi-objective aerodynamic optimization design of a high-speed train head under crosswinds. *Proceedings of the Institution of Mechanical Engineers, Part F: Journal of Rail and Rapid Transit* 232, 895-912.